3-27-2012

Spatial and spectral performance of a chromotomosynthetic hyperspectral imaging system

Randall L. Bostick
Air Force Institute of Technology

Glen P. Perram
Air Force Institute of Technology

Recommended Citation

Randall L. Bostick, Glen P. Perram; Spatial and spectral performance of a chromotomosynthetic hyperspectral imaging system. Rev Sci Instrum 1 March 2012; 83 (3): 033110. https://doi.org/10.1063/1.3697720

Review of Scientific Instruments

RESEARCH ARTICLE | MARCH 27 2012

Spatial and spectral performance of a chromotomosynthetic hyperspectral imaging system

Randall L. Bostick; Glen P. Perram

Rev Sci Instrum 83, 033110 (2012)
https://doi.org/10.1063/1.3697720

Spatial and spectral performance of a chromotomosynthetic hyperspectral imaging system

Randall L. Bostick and Glen P. Perram[a)]
Department of Engineering Physics, Air Force Institute of Technology, Wright-Patterson Air Force Base, Ohio 45433-7765, USA

(Received 23 December 2011; accepted 4 March 2012; published online 27 March 2012)

The spatial and spectral resolutions achievable by a prototype rotating prism chromotomosynthetic imaging (CTI) system operating in the visible spectrum are described. The instrument creates hyperspectral imagery by collecting a set of 2D images with each spectrally projected at a different rotation angle of the prism. Mathematical reconstruction techniques that have been well tested in the field of medical physics are used to reconstruct the data to produce the 3D hyperspectral image. The instrument operates with a 100 mm focusing lens in the spectral range of 400–900 nm with a field of view of 71.6 mrad and angular resolution of 0.8–1.6 μrad. The spectral resolution is 0.6 nm at the shortest wavelengths, degrading to over 10 nm at the longest wavelengths. Measurements using a point-like target show that performance is limited by chromatic aberration. The system model is slightly inaccurate due to poor estimation of detector spatial resolution, this is corrected based on results improving model performance. As with traditional dispersion technology, calibration of the transformed wavelength axis is required, though with this technology calibration improves both spectral and spatial resolution. While this prototype does not operate at high speeds, components exist which will allow for CTI systems to generate hyperspectral video imagery at rates greater than 100 Hz. [http://dx.doi.org/10.1063/1.3697720]

I. INTRODUCTION

Due to technological constraints, hyperspectral imagery (HSI) has traditionally been used to monitor static or, at most, events with slowly changing (>1 min) spatial and spectral features. However, there is considerable potential for exploiting features captured by HSI to characterize fast transient events, such as bomb detonations, muzzle flashes, and other battlefield combustion events.[1,2] Advances in technology have yielded several instrumental approaches for doing fast HSI, including two key technologies: imaging Fourier Transform Spectroscopy (imaging FTS) and chromotomosynthetic imaging (CTI) spectroscopy (which has also been referred to as chromotomography in the literature). Though significant advances have been made in FTS spectroradiometers,[3] CTI is investigated here due to anticipated advantages over FTS and other approaches, including: (1) simple design with less sensitivity to vibration, (2) easy integration with standard imaging sensors and technology, (3) high throughput similar to dispersive spectrometry constraints, (4) the flexibility to capture panchromatic imagery and perform high-speed non-imaging spectroscopy with the same dataset collected to produce the 3D spatial/spectral image cubes, and (5) speed of data collection is limited only by the detector readout and not by the piston movement. In chromotomosynthesis, a dispersive instrument collects convolved spatial and spectral information that can be reconstructed using the same transforms employed in medical tomography. One method features the use of a computer generated hologram (CGH) disperser to simultaneously produce a 5 × 5 array of diffraction orders onto a CCD detector array.[4–6] A second form of chromotomosynthesis utilizes a rotating direct vision prism to collect spectral projections at different prism rotation angles.[7,8] Due to the relatively low sensitivity, limited spectral range, and limited spectral resolution of the CGH, we have chosen to pursue a rotating prism CTI design. The prism CTI offers potentially higher SNR as a single projection is taken for a given integration time and uses the entire spatial extent of the detector array to collect one projection, offering increased spatial resolution and spectral resolution. For applications such as the classification of detonation events, the higher spectral resolution is required, as source spectra must be detangled from atmospheric transmission, and spectral fingerprints from hot combustion products, or incomplete fuel consumption, are key discriminating features.[1,2]

The rotating direct vision prism (DVP) design was most notably developed by Mooney *et al.* in connection with the Air Force Research Laboratory (AFRL).[8,9] A general description of the instrument with some component details are provided for the infrared version of the instrument.[8] A second Visible and Near Infrared (VNIR) instrument was also developed which is apparently more complex.[9] In neither case was the performance of the instrument in terms of spectral or spatial resolution provided, rather several examples of spectral measurements against static scenes are documented. Subsequent literature focuses on the system transform and mathematical reconstruction of the collected data sets.[8–13] The effects of instrumental design and performance parameters on temporal, spectral, and spatial resolution are not well documented. At the time of writing this paper, it is not clear that CTI can meet critical mission area requirements, nor is it

a)Author to whom correspondence should be addressed. Electronic mail: randall.bostick2@wpafb.af.mil. Tel.: (937)-656-0186.

known what effects such as jitter, field angle, and other instrument error has on the data collection or how these propagate through the data transform.

In this paper a prototype CTI instrument is presented. A short explanation of the data collection process and backprojection transform is then provided. Data are collected for an unresolvable 200 μm pinhole to represent a point-like source which is illuminated by 4 spectrally emitting sources (Ar, He, Ne, and Xe pen lamps) as well as a 1200 °C blackbody to measure the resolution of the system in the 2D space as one would a traditional dispersion spectrometer. Resolution is then measured in the 3D image cube to assess the effect of the transform. The results compare well to those predicted by a model of the system and transform mathematics with noticeable discrepancies attributable to error in knowledge of the forward transform of the system. The sources of error are identified and a methodology for system calibration is presented which is similar to that used in traditional prism spectroscopy. Our prototype is not a fieldable instrument, but one to be used specifically for assessment of metrology.

II. DESIGN OF THE CHROMOTOMOSYNTHETIC IMAGER

The basic CTI functionality is similar to that of the previous AFRL instrument[7,8] and is shown schematically in Fig. 1(a). The system features a DVP as the dispersion element (Fig. 1(b)), which is centered on and rotates about the optical axis. The entry telescope is formed by lens 1 and lens 2 (L_1 and L_2) and used to collimate the source rays input to the DVP and establish a well-defined incident angle. The aperture located at the image plane of L_1 defines the field of view (the field stop of the system). The dispersed light exiting the prism passes through a focusing lens (L_3) and is imaged onto the detector array, which is near the focal plane of L_3. The telescope angular field of view α is 71.6 mrad for a spatial field of view, a, of 100 mm for an object 1400 mm in front of the instrument. The focal lengths of the first two lenses are f_1 = 76.2 mm and f_2 = 250 mm, establishing a ratio of f_1/f_2 = 0.305. The final focusing lens has a focal length of f_3 = 100 mm. Though all lenses are achromatic doublets, the effective focus of the system has a noticeable wavelength dependence, which is optimized at about 650 nm.

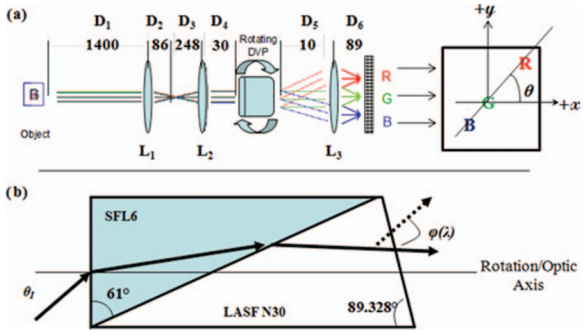

FIG. 1. (a) Schematic design of the CT instrument. L_1 and L_2 are afocal telescopes to collimate incoming light. The rotating DVP disperses light as a function of wavelength, and L_3 acts as a focusing lens to produce an image on the detector array. Distances, D, are in mm. (b) The material and geometry of the direct vision prism.

The detection array is a PI-MAX camera which features a proximity-focused microchannel plate Gen-II image intensifier fiber-optically coupled to a 1024 × 1024 pixel CCD array. The CCD is red-blue enhanced and has a maximum quantum efficiency of about 20% at 450 nm with responsivity from 200 nm to near 900 nm. The detector is thermoelectrically cooled to −10 °C and operated in shutter mode with variable exposure times. The camera is powered and controlled by an ST-133 controller connected to a computer for control and display. The 13 μm pixel pitch provides a total detection area of about 1.33 × 1.33 cm^2.

The DVP was purchased from Schott Glass and is fabricated from two glasses, with SFL6 being the entrance and LaSF-N30 being the exit material as illustrated in Fig. 1(b). The index of refraction for both SFL6 and LaSF-N30 at $\lambda = 619.29$ nm is $n = 1.8006$. The prism dispersion displaces the image some distance on the focal plane with respect to its location had the prism not been present. This distance, in terms of Δx and Δy displacement in focal plane space, is a function of the rotation angle of the prism, θ, the angular dispersion of the prism, $\varphi(\lambda)$, and the distance D_6 from the focus lens L_3 to the detector array and is given by

$$\Delta x(\lambda, \theta_p) = r(\lambda)\cos(\theta), \tag{1}$$

$$\Delta y(\lambda, \theta_p) = r(\lambda)\sin(\theta), \tag{2}$$

where

$$r(\lambda) = D_6 \tan(\varphi(\lambda)). \tag{3}$$

Because $r(\lambda)$ defines spectral performance of the system, the choice of f_3 and $\varphi(\lambda)$ are key system components. As noted, f_3 changes noticeably with λ despite use of achromatic doublets. Figure 2 shows a plot of $\varphi(\lambda)$ from a model of the DVP as well as the corresponding $r(\lambda)$. The undeviated wavelength, λ_c, is defined by $\varphi(\lambda_c) = 0°$, which occurs at about 548 nm. The detector array must collect energy from a defined object space of compact support, $f(x,y)$. In order that the space can be completely characterized in the case of limited spatial or spectral content, the field stop cannot be the detector array itself but must be limited such that $f(x,y)$ and its spectrally dispersed images are contained on the array for all θ. In terms of constraint on the design of the instrument, the displacement of a point cannot be so great that for any point

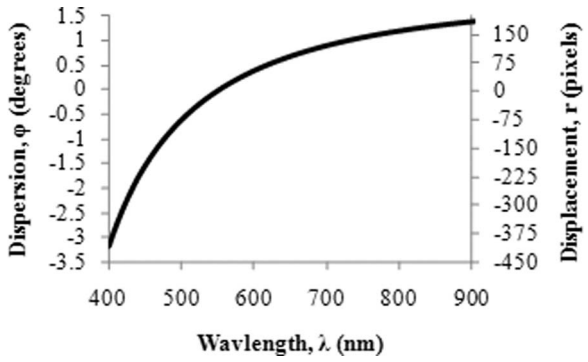

FIG. 2. The spectral displacement curve in terms of the angular spectral dispersion of the prism and the total displacement in pixels at the detector array for a 0° field angle.

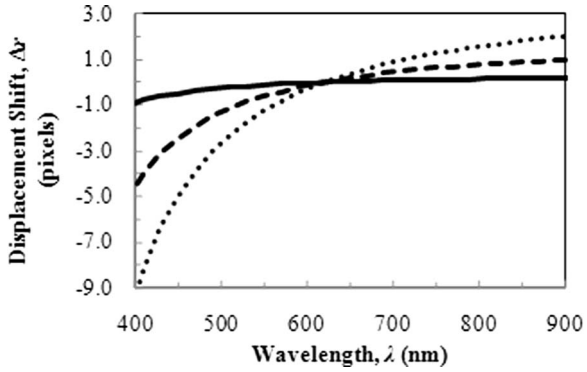

FIG. 3. The shift in displacement Δr at the array as a function of three input field angles θ_I to the prism; $\theta_I = 0.1^\circ$ (solid line), $\theta_I = 0.5^\circ$ (dashed line), and $\theta_I = 1.0^\circ$ (dotted line).

in the image space of $f(x,y)$, the desired spectrum of collection falls off of the detector array at any θ. With a desired coverage of 400–900 nm in spectral range, an $f_3 = 100$ mm lens was selected so that $r(\lambda)$ would be less than half the array length, with a margin of 200 pixels for the radius of the field of view. The prism linear dispersion is also shown in Fig. 2, with pixel displacement, $r(\lambda)$, plotted on the second axis.

Figure 3 shows the shift in pixel displacement, $\Delta r(\lambda)$, from that in Fig. 2 as a function of field angle, θ_I. Notice that for $\theta_I = 1^\circ$, the value for $r(\lambda = 400$ nm) is nearly 10 pixels different than for the center of the FOV where the $\theta_I = 0^\circ$. From Fig. 2, this would produce a registration error of approximately 2 nm, for the chosen $f_3 = 100$ mm lens. Though a smaller shift is incurred at higher λ, the lower prism dispersion results in an 8 nm error at $\lambda = 750$ nm. Unlike traditional spectroscopy, spatial blurring in the transformed 3D data would occur as a result of the systematic error in the knowledge of $r(\lambda)$. The relationship between the field angle θ_I, the field of view diameter at the object plane, α, and the focal lengths f_1 and f_2 is shown in Eq. (4).

$$\tan(\theta_I) = \frac{\frac{\alpha}{2} \times f_1}{(D_1 - f_1) \times f_2}. \tag{4}$$

To achieve a spectral resolution of 1 nm or less at $\lambda = 400$ nm with the design, θ_I must be less than 0.65°. For a reasonably distant object, this requires the ratio of f_1 and f_2 be ≤ 0.32. Using readily available lenses and maintaining a somewhat optically fast system, the combination of $f_1 = 75$ mm and $f_2 = 250$ mm was chosen. The lenses are separated by 334 mm to render the combination afocal and ensure that exit rays are parallel. All lenses are Thorlabs positive visible achromats with a diameter of 50.8 mm. The resulting optical chain gives a reasonable $f(x,y)$ (field of view) of about 100 mm in the object plane while maintaining favorable imaging parameters.

III. DATA RECONSTRUCTION

Several analytic and iterative data reconstruction methods are available, which are well documented and use the same mathematical processes to reconstructing imagery in medical computed tomography.[14,15] In tomosynthesis (unlike tomography), the rotation axis is not perpendicular to the dispersion axis and a number of discrete 2D exposures are collected. This incomplete set of data can be transformed to yield images similar to conventional tomography. However, the acute dispersion angle allows for a series of slices at different depths and with different thicknesses to be reconstructed from a single acquisition, saving time and minimizing patient exposure to radiation. The CTI spectral collection system has the same mathematical collection geometry and is thus most similar to circular tomosynthesis.[16–19] Because the projection angle in CTI is small ($<10^\circ$) the direct inversion of the system transformation is nearly singular and, as Mooney points out,[8,9] complicated mathematical methods are required to estimate a direct solution. More suitable algorithms have been developed for clinical use in circular tomosynthesis.[20–23] An algorithm based on back projection of the data was used in this study and described below. It is a simple algorithm and is generally the starting point for any of the other higher level algorithms which optimize performance based on specific application or known systematic errors in circular tomosynthesis.

A projection $P(x,y,\theta)$ is defined as the 2D sample of the detector array at any prism rotation angle θ. Generally, the projections are filtered in frequency space to compensate for the blurring effects of the back projection process, referred to as Fourier Back Projection.[14,15] Because the test objects here are simple and all bins are sampled with the same spatial resolution, an unfiltered back projection technique is used. With this method the image at any wavelength bin λ can be reconstructed from a set of projections taken over $0^\circ < \theta_p < 360^\circ$ with resolution dependent on the spatial resolution of the system and density of samples. For any $P(x,y,\theta)$, the spatial data in the 2D is described in terms of the object as

$$P(x, y, \theta) = I_0(x + \Delta x(\lambda, \theta), y + \Delta y(\lambda, \theta)), \tag{5}$$

where $I_o(x,y)$ is the image as it would appear without any prism dispersion. With the linear shifts $\Delta x(\lambda,\theta)$ and $\Delta y(\lambda,\theta)$ established from Eqs. (1)–(3), an estimate of $I_o(x,y)$ at any λ denoted by $I_p(x,y,\lambda,\theta)$ can be calculated from $P(x,y,\theta)$ by reversing the shift so that the energy is placed back at its original position in image space. Because $\Delta x(\lambda,\theta)$ and $\Delta y(\lambda,\theta)$ are rarely integers, the value assigned to a particular point in $I_p(x,y,\lambda,\theta)$ will be the value of a pixel multiplied by the fraction of the area of overlap upon shifting (x,y) by some real-valued $\Delta x(\lambda,\theta)$ and $\Delta y(\lambda,\theta)$. If $a - (x - \Delta x(\lambda,\theta), y - \Delta y(\lambda,\theta), x', y')$ represents this fractional overlap then

$$I_p(x, y, \lambda, \theta) = \sum_{x', y'} P(x - \Delta x(\lambda, \theta), y - \Delta y(\lambda, \theta)) \times a(x - \Delta x(\lambda, \theta), y - \Delta y(\lambda, \theta), x', y'). \tag{6}$$

A complete reconstructed image cube $R(x,y,\lambda)$ for all projections is estimated from the weighted summation over all θ and λ as shown in Eq. (7),

$$R(x, y, \lambda) = \frac{1}{N} \sum_{\theta, \lambda} I_p(x, y, \lambda, \theta). \tag{7}$$

In any particular spectral bin λ_n the spatial data at that wavelength is co-added such that the spatial information is reinforced. Spatial information from other spectral bins are also included, but for $\lambda \neq \lambda_n$ the information is not coherently added and appears blurred in $R(x,y,\lambda_n)$. For complex spectral and special data, additional image process would be needed to discern or remove these artifacts.[20–22] From Eq. (6) it is obvious that systematic error in knowledge of $\Delta x(\lambda,\theta)$ and $\Delta y(\lambda,\theta)$ results in variations between I_p and I_0. Depending on the type of error, this results in either a loss of spatial resolution at a particular wavelength, a shift in the peak spectral location, or both in the final $R(x,y,\lambda)$. An additional loss of resolution occurs as the back projection process essentially is resampling the data, which mathematically represents a second convolution with the detector array. Some of these differences can be rectified and the original resolution restored by using more advanced drizzle techniques to recombine the shifted datasets,[23] or, as is commonly done in medical CT, filtering the data prior to backprojection. Reconstruction algorithms utilize $\Delta x(\lambda,\theta)$ and $\Delta y(\lambda,\theta)$ as input, and thus the accuracy of the data reconstruction is dependent on knowledge of system performance.

IV. EXPERIMENT

To measure the spatial point response function (PRF) and spectral line shape function (LSF) of the CTI, a 200 μm diameter pinhole is illuminated as the object for the CTI system. The image size predicted by geometric optics is a circle of diameter 4.6 μm, about 1/3 of a pixel. The pinhole was illuminated separately by argon, mercury, neon, and xenon pen lamps and a 1200 °C black body. The spectral peak locations for lines used in this analysis are given in Table I, taken from a combination of the lamp documentation[24] and the NIST database.[25] To acquire data at shorter wavelengths, a second collection of the black body was made with a 500 nm short pass filter in place. This allowed the integration time to be increased to detect energy at the shorter wavelengths while avoiding extreme saturation and artifacts from scattered light from the longer wavelengths.

For the spectral sources a single measurement was made by the CTI without the prism in place to determine a reference point for the undeviated image location, or $r(\lambda = \lambda_c)$. Four measurements of $P(x,y,\theta)$ with the prism in place at $\theta = 0°$, 90°, 180°, and 270° were made for the spectral and black body sources. The $P(x,y,\theta)$ data of the spectral sources were transformed into the reconstructed 3D space, $R(x,y,\lambda)$. The bin size for the reconstructions was 0.1 nm over 400–500 nm for each source and 0.5 nm from 500 to 800 nm due to lower spectral resolution of the instrument at the longer wavelengths.

The spectral intensity of each of the Ar, Hg, Ne, and Xe sources is extracted from each of the four $P(x,y,\theta)$ by integrating the center 4 rows or columns (as appropriate) around the center line of the spectra. This resulted in an intensity plot vs. pixel location for the 2D instrument collection space which was converted to intensity vs. wavelength using the predicted performance and measured $r(\lambda)$ using the undeviated images. The average of the $P(x,y,\theta)$ were taken to provide a single spectrum for each element in the 2D collection space. The spectra for the $R(x,y,\lambda)$ were extracted by integrating the 2×2 pixel area at the center of the image location at every reconstructed plane. The widths of peaks in the direction perpendicular to the dispersive axis of the DVP were used to obtain spatial resolution. In the 3D reconstructed data, spatial resolution was measured in both the x- and y-axis in the plane of peak spectral intensity.

Peak center locations and PRF/LSF functional fits were estimated by fitting the collected data to a Gaussian line shape. With a few exceptions, the Gaussian shape was the best functional fit to the data with an r-squared fit coefficient of >0.99 for all peaks used in the assessment. The FWHM of the Gaussian shapes were then calculated to find the spatial/spectral resolution. Contributions from instrument bias, background, or continuum energy in the spectra were removed prior to fitting. An example of the fit to the Ne spectrum is shown in Figure 4 plotted with peaks extracted from the data.

TABLE I. Prominent pen lamp wavelengths (nm).

Ar	Ne	Hg	Xe
404.44	585.25	404.65	450.1
415.86	588.19	435.83	452.1
416.42	594.48	546.08	453.25
418.19	609.62	576.96	462.4
419.81	615.34	579.07	467.1
425.94	621.73		469.8
426.63	626.65		473.4
430.01	633.44		480.7
433.41	640.16		482.97
434.51	650.65		491.95
451.07	660.1		502.83
452.23	667.8		
	671.7		
	692.25		
	702.83		
	724.52		
	748.89		

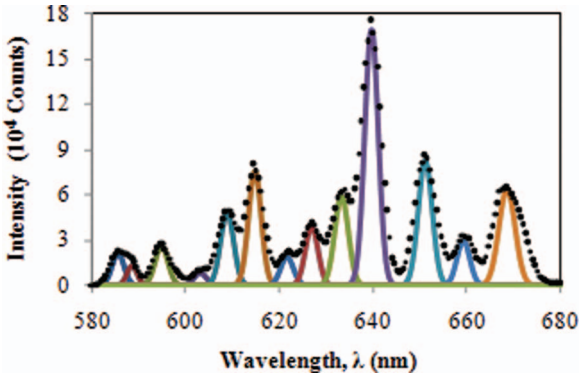

FIG. 4. An example of the peaks fit to the extracted Ne spectrum in the 3D reconstructed imagery. The dotted line is the data; the solid line represents the fitted peaks.

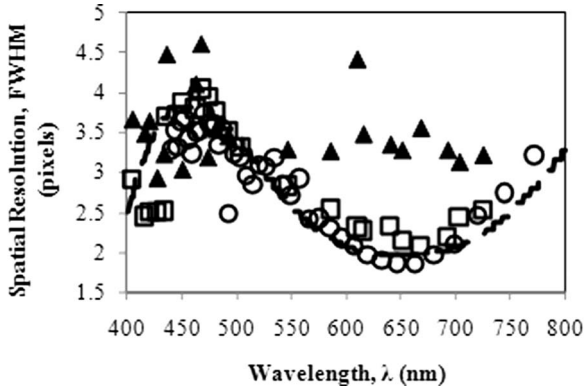

FIG. 5. The spatial resolution results for the black body source (**o**), spectral sources (□), and the measured spatial resolution in the 3D reconstructed data (▲). The dashed curve is the predicted resolution from the model of the system after adjusting for the detector coupling.

V. RESULTS

A. Spatial resolution

The wavelength dependence of the observed spatial resolution of the collection system in the $P(x,y,\theta)$ for both the pen lamps and the black body are illustrated in Fig. 5. The spatial resolution varies from 2–4 pixels or 26–52 μm. This corresponds to an object resolution of 0.8–1.6 μrad or 1.2–2.4 mm for an object at 1400 mm from the instrument. The best spatial resolution of 2.05 pixels is observed at $\lambda = 650$ nm, the wavelength at which system focus is optimized. The average of the PSF in the x- and y-directions of the $R(x,y,\lambda)$ reconstructed data are also plotted in Fig. 5. The resolution is constant across the spectral range at about 3.4 pixels. This indicates that there is residual error in the estimation of $\varphi(\lambda)$ which dominates the performance in the $R(x,y,\lambda)$.

The overall shape of the curve of the PRF as a function of λ indicates that the performance of the system is limited by chromatic aberration, as the effective focal length, f_s, of the system depends on λ. A model of the image system is developed to support this conclusion. Four components were assumed main contributors to the overall PRF of the system: diffraction, detector sampling, effect of the intensifier, and chromatic aberration. The (assumed circular) prism is the limiting aperture of the system and the diffraction term is described by an Airy disk with radius:

$$d(\lambda) = 1.22 \times \frac{f_s \times \lambda}{A_p}, \tag{8}$$

where A_p is the aperture size of the prism (21 mm) and f_s is assumed equivalent to f_3 assuming that the front telescope is afocal (this is not explicitly true given the achromaticity of the system). The radius of the diffraction circle is $d \approx 4.7$ μm at $\lambda = 800$ nm, just over 2/3 of a pixel in total diameter for the spectral range of interest.

Sampling due to physical spatial detector size was modeled as constant, 1 pixel wide *rect*(*x*) function. The PI-MAX camera has an intensified array and the pixel pitch will not alone define the spatial sampling resolution of the system. Incident photons excite the photocathode, which causes a release of electrons that are attracted to the voltage biased microchannel plate that acts as the photomultiplier. The exited high-energy electrons strike a fluorescent screen to create the photons that are incident on the CCD. The fiberoptic coupling between the photocathode and CCD array introduces a FWHM blur diameter documented to be about 45 μm[26] (or nearly 3.5 pixels). The coupling contribution to the PSF is modeled as a Gaussian function to produce the required FWHM.

It was also necessary to consider chromatic aberration as the λ dependent effects were easily observed in initial data sets. The distances between lenses were fixed to provide best focus at $\lambda = 650$ nm. In particular, $D_6 = 89$ mm which can be most easily adjusted if improved resolution is desired at different λ. At this wavelength f_1 and f_2 form an afocal telescope so that $f_s = f_3$. The effective focal length of each lens was then modeled to determine image quality over the full range of λ. The blur size of the image of a point source was then modeled using geometric optics over the spectral range and was found to be approximated as a uniform disk, such that it is represented by a *circ*(*r*) function. The size of *r* was estimated as half the distance between marginal rays at the fixed distance D_6 from back face of L_3.

Complete spatial resolution in the $P(x,y,\theta)$ data was approximated by convolving the four effects described. The spatial resolution in any 3D $R(x,y,\lambda)$ bin (assuming perfect reconstruction) was found by incorporating the additional pixel sampling factor as a result of the back projection algorithm. The estimation of the FWHM of the PSF in the $P(x,y,\theta)$ and $R(x,y,\lambda)$ space are shown in Fig. 6. There is a small difference between the two, with the minimum spatial resolution dependent on the intensifier fiber coupling and added modulation due to chromatic aberration.

Comparing the model results with the data in Figure 5, the measured shape and amplitude of the system resolution agrees well with the model, but the minimum of the curve at 650 nm is much lower at a FWHM of 2 pixels compared to the predicted 3.5 pixels. This indicates that the estimated intensifier coupling term is too high. Adjusting this term to have a FWHM of 1.9 pixels (24 μm) produces a predicted spatial resolution that is much closer to the data as indicated in Fig. 5 by the dashed adjusted model curve.

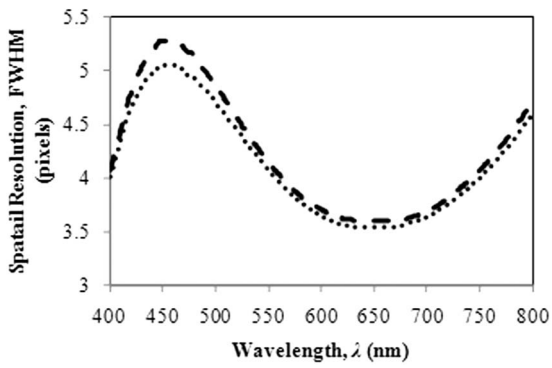

FIG. 6. The expected PRF from the model of the system. The spatial resolution of the collection system is shown as the dotted line. The spatial resolution in the reconstructed 3D hyperspectral data is shown as the dashed line.

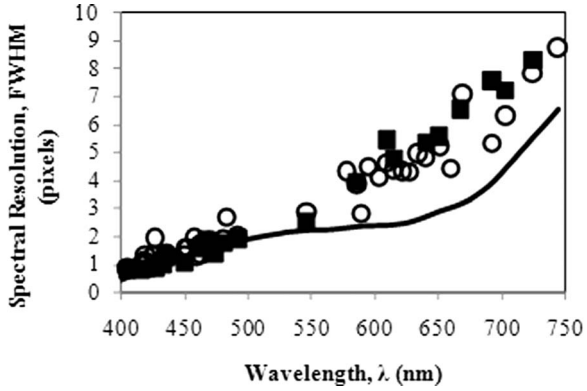

FIG. 7. The measured spectral resolution from the 3D $R(x,y,\lambda)$ data (**o**), the predicted spectral resolution from the system (solid line), and the expected resolution given estimated error in reconstruction (■).

B. Spectral resolution

The measurements of the LSF for the spectral sources indicate that the system is capable of providing a spectral resolution $\Delta\lambda$ of about 0.75 nm at 400 nm, rising fairly linearly to nearly 9 nm at 750 nm. The results are shown in Fig. 7 with the line indicating the theoretical best spectral resolution derived from the model-based spatial resolution. This dependence can be shown to have the same relationship that exists in prism spectroscopy, where

$$\Delta\lambda_m = \frac{w}{f_3(\lambda) \times \frac{d\varphi(\lambda)}{d(\lambda)}} \tag{9}$$

with $\Delta\lambda_m$ being the minimum spectral resolution and w is the spatial resolution. At $\lambda < 550$ nm, the measured width of the LSF is near the theoretical limit and considerably higher at the longer wavelengths.

The deviation from the model above 550 nm is where the spatial resolution was found to be worse in the reconstructed data compared to the systematic and modeled spatial resolution. Thus, as in traditional 2D spectroscopy, the spectral resolution in the $R(x_i,y_i,\lambda)$ space is dependent on the spatial resolution *in this same space*, not the projection space. By using the measured spatial resolution in the 3D data set as the basis for the predicted spectral resolution instead of the modeled spatial resolution, values much closer to those measured are found as shown in Fig. 7.

C. Spectral registration and calibration

The system spatial performance is well known and modeled but some error exists in the predicted spectral dispersion of the system, as the measured performance in the reconstructed hyperspectral data is not as good as predicted. The error caused by differences between the model and reality can be quantified by examining the location $r(\lambda)$ of the spectral point source images on the array for each θ and compared to the model. Figure 8 plots the expected $r(\lambda)$ due to dispersion from the model, with the measured peak center locations of the spectral source images at $\theta = 0°$, 90°, 180°, and 270° overlaid. The displacement error increases linearly with wavelength with some random error. By incorporating a single linear correction, Fig. 9 shows that the residuals are now scattered mostly about $\Delta r = 0$, with a slight overall bias of about 0.2 pixels.

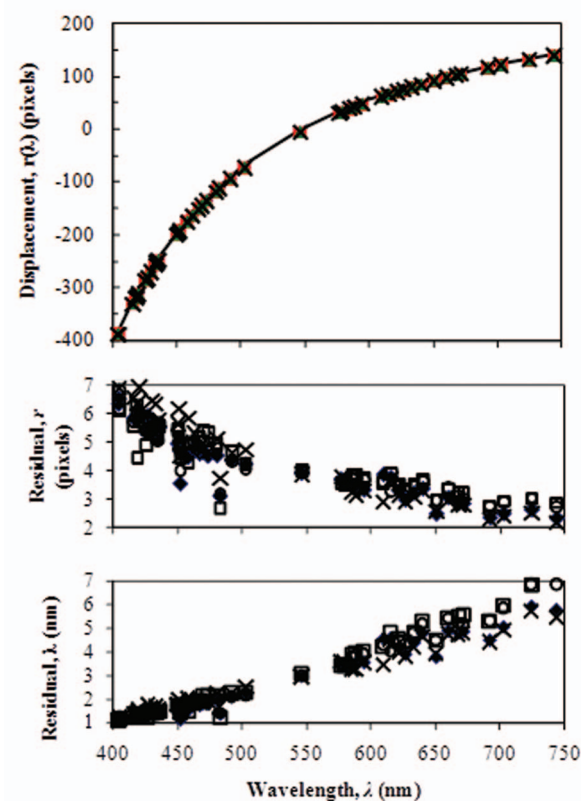

FIG. 8. The predicted spectral displacement $r(\lambda)$ compared to that measured in the $P(x,y,\theta)$ sets: $\theta = 0°$ (♦), $\theta = 90°$ (□), $\theta = 180°$ (o), and $\theta = 270°$ (x). Residuals in terms of pixels and wavelength, λ, are shown below the plot with a noticeable correlation between the $P(x_i,y_i,0°)$ and $P(x_i,y_i,90°)$ data and the $P(x_i,y_i,180°)$ and $P(x_i,y_i,270°)$ data.

It is clear from Figs. 8 and 9 that the error is more apparent for results at $\lambda > 550$ nm, where poorer agreement between the measurements and the model were observed. The sensitivity to decreased $d\lambda/dr$ causes higher inaccuracy per λ

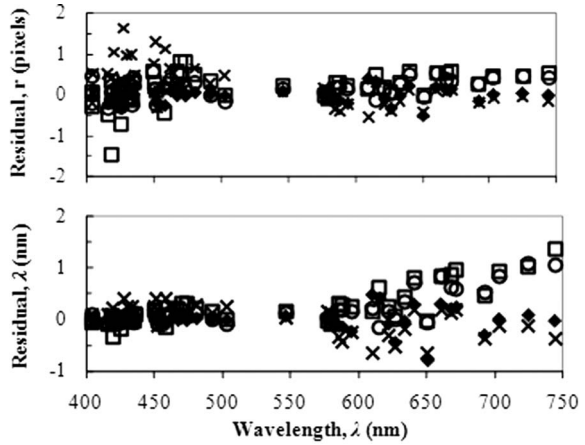

FIG. 9. The residuals between the measured and modeled dispersion after a linear correction is applied based on measurements of the spectral dispersion in the data used in this experiment. The symbols are the same as those in Figure 8.

at these wavelengths, as a larger change in λ is produced for an equivalent change in r. Most outliers contributing to the randomness in Δr is likely caused by noise in the data, effects of under sampling the PSF, the presence of the continuum, overlapping peaks or difference in emission spectra between the pen lamps used and/or documented emission lines. The remaining bias is evident in the correlation between the 0° and 90° and the 180° and 270° projections. Applying distinct linear corrections to each of the projections would further improve the performance, with a complete calibration that describes spectral displacement in terms of $r(\lambda,\theta_p)$ necessary. The single linear correction improves spatial results by 25% and spectral by 10%.

VI. CONCLUSIONS

A prototype CTI instrument has been designed, built and characterized which broadly covers visible wavelengths from 400–900 nm with spectral resolution of 0.6–10 nm depending on wavelength. The compact, $f = 100$ mm, instrument provides hyperspectral images with per pixel field of view of 0.6 mrad and a full field of view of 71.6 mrad. A simple back projection algorithm for image reconstruction does not significantly degrade the native spatial and spectral resolution when the system linear dispersion and other instrument properties are adequately characterized. Indeed, system performance is primarily limited by chromatic aberrations for the transmissive optics. The distance between the back lens and the detector array can be adjusted to minimize blur at a desired wavelength.

Unlike normal dispersive spectrometers, CTI cannot dramatically improve spectral resolution by simply increasing the focal length, except near the undispersed wavelength. This is because the image of the field of view must be rotated for all wavelengths. However, resolving the visible spectrum into several hundred bins can be achieved with the $f = 100$ mm system. Calibration of the wavelength axis is required for absolute wavelength determinations and also improves the resulting spectral resolution. Calibration may be necessary for all rotation angles.

Further development of the CTI instrument is required for objects with more diverse spatial frequencies. In particular, the sensitivity of reconstructed images to systematic errors for scenes with increased spatial and spectral mixing must be developed. Extension to a fast framing, field deployable system is in progress.[27] Many factors affect the achievable spatial and spectral resolution attainable from an operational CTI system. More specifically, the contrast values that define the ability to detect and resolve spatial features at a given wavelength require further study.

[1] Kevin C. Gross, Glen P. Perram, and Ronald F. Tuttle, Proc. SPIE **5881**, 100 (2005).
[2] J. A. Orson, W. F. Bagby, and G. P. Perram, Infrared Phys. Technol. **44**, 101 (2003).
[3] K. C. Bradley, K. C. Gross, and G. P. Perram, Proc. SPIE **7304**, 73040J (2009).
[4] M. Descour and E. Dereniak, Appl. Opt. **34**, 4817 (1995).
[5] M. R. Descour, C. E. Volin, E. L. Dereniak, and K. J. Thome, Opt. Lett. **22**(16), 1271 (1997).
[6] M. R. Descour, C. E. Volin, E. L. Dereniak, and K. J. Thome, Appl. Opt. **36**(16), 3694 (1997).
[7] B. K. Ford and M. R. Descour, Opt. Express **9**(9), 444 (2001).
[8] J. M. Mooney, Proc. SPIE **2480**, 65 (1995).
[9] J. E. Murguia, T. D. Reeves, J. M. Mooney, W. S. Ewing, F. D. Sheperd, and A. Brodzik, Proc. SPIE **4208**, 457 (2000).
[10] A. K. Brodzik and J. M. Mooney, J. Opt. Soc. Am. **16**(2), 246 (1999).
[11] K. C. Gustke, Master's thesis, Air Force Institute of Technology, 2004.
[12] M. Gould and S. Cain, Opt. Eng. **44**, 1111 (2005).
[13] D. A. LeMaster, Master's thesis, Air Force Institute of Technology, 2004.
[14] R. A. Brooks and G. Di Chiro, Phys. Med. Biol. **21**(5), 689 (1976).
[15] J. Hsieh, *Computed Tomography: Principles, Design, Artifacts, and Recent Advances* (SPIE, Washington, 2003).
[16] U. E. Ruttimann, R. A. Groenhuis, and R. L. Webber, IEEE Trans. Med. Imaging **3**(3), 141 (1984).
[17] J. B. Garrison, D. G. Grant, W. H. Guier, and R. J. Johns, "Three-Dimensional Roentgenography," Amer. J. Roentgenol. **105**(4), 903 (1969).
[18] D. G. Grant, IEEE Trans Biomed. Eng. **1**, 20 (1972).
[19] R. J. Warp, D. J. Godfrey, and J. T. Dobbins, Proc. SPIE **1**(22), 376 (2000).
[20] J. T. Dobbins and D. J. Godfrey, Phys. Med. Biol. **48**, R65 (2003).
[21] H. Matsuo, A. Iwata, I. Horiba, and N. Suzumura, IEEE Trans. Med. Imaging **12**(2), (1993).
[22] G. M. Stevens, Med. Phys. **28**(3), 372 (2001).
[23] A. S. Fruchter and R. N. Hook, Publ. Astron. Soc. Pac. **114**, 144 (2002).
[24] L.O.T.-Oriel UK, "Pen-Ray Line Sources," Leatherhead, Surrey, UK.
[25] National Institute of Standards and Technology, NIST Atomic Spectra Database Lines Form, 2008, see http://physics.nist.gov/PhysRefData/ASD/lines_form.html.
[26] *PI-MAX/PI-MAX2 System User Manual* (Princeton Instruments, New Jersey, 2004).
[27] D. C. O'Dell, R. L. Bostick, M. R. Hawks, E. D. Swenson, J. T. Black, R. G. Cobb, and G. P. Perram, Proc. SPIE **7668**, 766804 (2010).